Comput Mech (2012) 50:209–227
DOI 10.1007/s00466-012-0724-8

ORIGINAL PAPER

An integrated 2-D model of a lithium ion battery: the effect of material parameters and morphology on storage particle stress

Rajlakshmi T. Purkayastha · Robert M. McMeeking

Received: 16 April 2012 / Accepted: 18 April 2012 / Published online: 15 May 2012

Abstract An integrated 2-D model of a lithium ion battery is developed to study the mechanical stress in storage particles as a function of material properties. A previously developed coupled stress-diffusion model for storage particles is implemented in 2-D and integrated into a complete battery system. The effect of morphology on the stress and lithium concentration is studied for the case of extraction of lithium in terms of previously developed non-dimensional parameters. These non-dimensional parameters include the material properties of the storage particles in the system, among other variables. We examine particles functioning in isolation as well as in closely-packed systems. Our results show that the particle distance from the separator, in combination with the material properties of the particle, is critical in predicting the stress generated within the particle.

Keywords Lithium ion battery · Coupled stress-diffusion model · Non-dimensional parameters · Numerical simulations

R. T. Purkayastha (✉) · R. M. McMeeking
Materials Department, University of California, Santa Barbara, Santa Barbara, CA 93106, USA
e-mail: rajlakshmi@engineering.ucsb.edu

R. M. McMeeking
Department of Mechanical Engineering, University of California, Santa Barbara, Santa Barbara, CA 93106, USA

R. M. McMeeking
School of Engineering, Aberdeen University, King's College, Aberdeen AB24 3UE, Scotland, UK

R. M. McMeeking
INM—Leibniz Institute for New Materials, Campus D2 2, 66123 Saarbrücken, Germany

1 Introduction

Ageing in lithium ion batteries has been a source of growing concern, given the rapid increase of their use, both in numbers and variety of devices. Ageing manifests itself primarily as capacity fade, power fade, increase in impedance and an overall decrease in performance [1,2]. Most ageing mechanisms are associated with reactions with the electrolyte and its organic solvent that cause decomposition, and the production of volatile and combustible gases, along with the generation of pressure that may rupture the cell container [3–6]. In addition, there can be effects indirectly related to the electrochemistry of the cell, such as corrosion of components of the electrodes, including the current collector, oxidation of conductive particles within the electrode and its binder, and binder decomposition, especially at high charging voltages [3–5].

The contribution of structural degradation to the ageing of batteries has become important as an increase of the lifetime of batteries is sought. There are two main causes of structural degradation. At high rates of charging and discharging, structural disordering and phase changes in the electrode storage materials may occur [6], resulting in slowing of the rate at which lithium can be inserted and extracted, and also diminishing the capacity of the cell. The second source of damage is the expansion and contraction of storage particles as Li^+ ions are extracted and inserted. In many storage materials, usually transition metal oxides, the process of removing or inserting lithium ions out of and into storage particles is by intercalation, formally defined as the insertion of a guest species into normally unoccupied interstitial sites in the crystal structure of an existing stable host material [1]. Depending on which material is used, as much as 100 % of the lithium is depleted from cathodes during charging [4], leading to significant shrinkage. For example, in $LiMn_2O_4$, depletion of

lithium to 20 % of stoichiometry leads to a volume reduction of 6.5 % [7]. Upon very fast charging, the first batch of lithium extracted from the oxide particle will deplete from near its surface, causing a high tensile hoop stress there as the outer layer shrinks. The resulting stress can cause cracks to propagate and damage the material. Thus, comminution of oxide particles in the cathode can occur during charging [1,7,8], a damage mechanism that can also accumulate by fatigue upon repeated cycling of the battery. One way of approaching the problem is to design newer materials with reduced valume changes [9]. There have been several attempts at applying fracture mechanics to these problems in order to predict conditions conducive to cracking [10–14] and criteria suggested to avoid it [15–18].

A good starting point for such studies is to consider a storage particle in isolation. Christensen and Newman [7] developed a multi-component diffusion model for estimating the stress generated in $Li_xMn_2O_4$, where they included the volume change during phase transformation. Pressure was used to account for the stress generated by swelling within the particle. Sastry and co-workers [19] developed a model based on a thermal analogy for stress, and also took into account the effect of different shapes of the particle as well as phase changes [20]. Cheng and Verbrugge [21,22] formulated analytical models within the particle for calculating the diffusion induced stresses (DIS) based on lithium concentration within the particle, but did not include any influence of the mechanical stress on diffusion of the lithium. Bohn et al. [23] developed a simulation for the diffusion within the particle based on a model for the lithium chemical potential encompassing the effect of stress and an excess Gibbs free energy. As a result they are able to simulate the effect of phase change and staging in storage particles.

Building on the model of Bohn et al. [23], we previously developed a set of non-dimensional parameters that can be used to characterize the stress response of any particle [24,25]. These parameters depend on material properties such as Young's modulus, lithium partial molar volume, and storage particle radius, among others. Performance maps generated for the case of extraction and insertion [24,25] show that high stress actually aids the process of lithium diffusion within the particle, acting in conjunction with the lithium concentration profile. More importantly, the maps, based as they are on dimensionless parameters, can be used for any storage material, subject to the caveat that they were developed only for spherical particles.

However, a storage particle in a lithium ion battery does not exist in isolation, but is a component of a large complex system of interacting species. Attempts to model the system in its entirety generally invoke reductions in the system complexity through the use of approximations in regard to the microstructure and other properties. As an example, porous electrode theory [26] has been extensively used to represent the complex microstructure of the battery in a 1-D approximation [7,27,28]. This has lead to 'pseudo-2-D' models, in which a single particle is coupled to a battery simulator based on porous electrode theory [23,29,30]. However, interactions among particles are inevitably omitted in such treatments. High local stress and lithium concentration caused by such interactions can be critical to the development and propagation of cracks [11,14,15].

Garcia et al. [31,32] studied stresses within an electrode using a 2-D model, in which the entire electrochemistry of the battery was modeled including storage particles, binder and electrolyte pores. These simulations clearly show the importance of particle position within the electrode, and corroborate other work [30] that shows that the closer the particle is to the separator the more stress it is likely to experience. However the model of Garcia et al. [31,32] does not couple diffusion with stress as a driving force. Furthermore, Wang and Sastry [33] modeled an entire battery system in 3-D; however they did not consider stress in their system.

In this work we extend our 1-D model to 2-D and apply it to a battery system. In order to avoid multiple competing effects we first consider an array of particles, equidistant from the separator. Our goal is to study the effect of particles on each other, and to investigate whether material parameters have an influence on the stress response. We then modify the cathode and add additional particles to the system. Our coupled model with 2-D simulations allows us not only to analyze the effect of different material parameters on the stress response within the particle but also to investigate local variations of lithium concentration and stress caused by particle interactions.

2 Model formulation

2.1 Lithium ion battery: operation

Figure 1 shows a schematic of the 2-D model we use for a lithium ion battery. There are two electrodes, the anode in the form of metallic lithium (Region I) and the cathode (Regions III and IV), consisting of storage particles (IV) and a composite, porous binder (III). The cathode is connected to a metal plate known as the current collector. As the anode comprises lithium metal, no current collector is needed for it. A porous polymeric component known as the separator lies between the two electrodes (Region II). The composite cathode consists of cylindrical storage particles (Region IV) surrounded by a porous binder, with electrolyte in its pores and in those of the separator. The entire system has uniform thickness, including the particles, and so is planar. Such geometry is artificial, as storage particles are usually 3-D, in spherical, ellipsoidal or acicular shapes. For the cathode, these particles normally consist of layered oxides, such as lithium manganate and lithium cobalt oxide. Compared

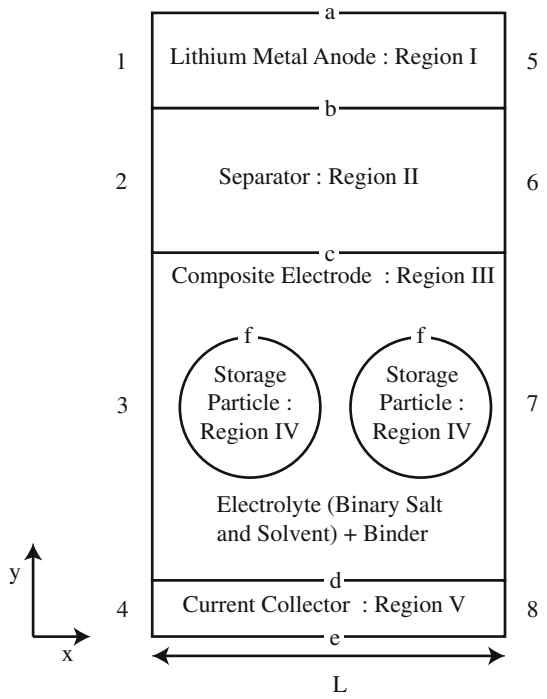

Fig. 1 A schematic of the lithium ion battery with two particles showing the different components

to the set-up in Fig. 1, cathode particles are usually more densely packed, with weight fractions of around 85 %.

The cell comprises two different conducting paths, one for lithium ions and the other for electrons. During battery discharge, electrons flow in and from the anode through an external lead (not shown in Fig. 1, but connecting a to e) to the current collector, and thence towards the cathode storage particles via a percolating network, usually carbon coated on binder and storage particles. At the same time, lithium is oxidized to Li^+ ions at the anode-separator interface at b in Fig. 1, and these ions are then transported through the electrolyte in the separator and cathode pores until they reach the surface of storage particles at f. There the ions are reduced to lithium once more, enter the particles, and are diffused through and stored within them. During charging of the battery, the motion of the electrons and the Li^+ions is reversed.

Our model of Region III in the cathode, consisting in reality of binder particles, pore space with electrolyte, and a carbon coating on the binder and storage particles, is that of storage particles surrounded by electrolyte, as if the binder particles are not present. Such an arrangement is a convenient simplification, and inert binder particles will be introduced in future. However, overlaid on the electrolyte pool in our model, but electrically isolated from it, is a homogenized path to give electrons access to the storage particles, this being a substitute for the percolating carbon network coated on binder and storage particles. This electron path is given a homogenized, effective conductance, as described below.

The electrolyte, normally consisting of a mixture of a binary salt, e.g. $LiPF_6$, dissolved in an organic solvent, is assumed to have zero net velocity, as for a solid electrolyte.

Nomenclature: In the next few sections we describe the formulation for transport of the various species in the battery. Since there are many different components we identify them as follows:

- The major regions of the battery (anode, separator etc.) are numbered with Roman numerals I, II etc. Terms belonging only to a particular region are indicated by a Roman numeral as a subscript
- The sides of the battery to which periodic boundary conditions are applied are numbered with decimal numbers 1, 2 etc.
- The boundaries between the different regions are labeled using lower case letters a, b, c etc. Terms used to describe quantities at the boundary regions are designated by a lower case letter as a subscript.
- Points within the system are referred to by capital letters A, B, C etc.
- Terms that are underlined are vectors.
- The subscripts + and − refer, respectively, to positively and negatively charged species.

2.1.1 Lithium transport in the electrolyte

We first consider the formulation governing transport of the various species in the electrolyte. We start with the transport equations for a binary salt in a solvent [26], given by

$$\underline{N}_+ = -\nu_+ \tilde{D} \underline{\nabla} c + \frac{t^o_+ \underline{i}}{z_+ F} + c_+ \underline{v}_o \tag{1a}$$

$$\underline{N}_- = -\nu_- \tilde{D} \underline{\nabla} c + \frac{t^o_- \underline{i}}{z_- F} + c_- \underline{v}_o \tag{1b}$$

where $\underline{N}_+$ is the flux of the positive ions in moles per unit area per unit time, $\underline{N}_-$ is the flux of the negative ions, ν_+ is the number of positive ions that are ionized from one molecule of salt, ν_- is the number of negative ones. In the case of the monovalent salts that we assume here for the electrolyte, $\nu_+ = \nu_- = 1$. The effective diffusion coefficient is

$$\tilde{D} = \frac{c_T}{c_o} D \left(1 + \frac{d \ln f_{+-}}{d \ln c}\right) \tag{2}$$

where the concentration c_T is the total concentration of the electrolyte in moles per unit volume, given by

$$c_T = c_o + c_+ + c_- \tag{3}$$

where c_o is the concentration of the solvent, c is the concentration of the salt, and therefore, the concentration of the positive ions is given by $c_+ = \nu_+ c$ and that of the negative ones by $c_- = \nu_- c$. The parameter f_{+-} is an activity coefficient for the ionized, dissolved salt, associated with non-ideal

Table 1 Geometrical parameters [28,31,33]

Parameter	Value (μm)
Anode length	50
Separator length	50
Cathode length	174
Current collector length	10

solution thermodynamics, and D is the diffusion constant of the salt in the solvent. In Eq. (1), i is the current density given by

$$\underline{i} = -\kappa \underline{\nabla}\Phi + \frac{\nu t_-^o}{\nu_+ z_+}\left(1 + \frac{d\ln f_{+-}}{d\ln c}\right)\frac{RT\kappa}{Fc}\underline{\nabla}c \tag{4}$$

and t_j^o is the transference number of species j in the solvent, giving the fraction of the current carried by that species. Thus, the sum of the transference numbers of all charged species in a solution is unity. In addition, z_+ is the charge number for a single positive ion and z_- is the charge number for one negative ion. Due to charge neutrality of the salt,

$$\nu_+ z_+ + \nu_- z_- = 0 \tag{5}$$

in all cases for a binary salt. The symbol F is Faraday's constant, giving the charge on 1 mole of protons, and $\underline{v}_o$ is the mass average velocity of the electrolyte, taken to be zero in our simulations. In Eq. (4), κ is the conductance of the electrolyte, Φ is its potential as measured by a reference electrode, the parameter ν is such that

$$\nu = \nu_+ + \nu_- \tag{6}$$

R is the gas constant, and T is the absolute temperature.

Conservation of charge in the electrolyte provides

$$\underline{\nabla}\cdot\underline{i} = 0 \tag{7}$$

and after this is taken into consideration, and given zero velocity of the electrolyte and uniform electrolyte properties, conservation of mass leads to

$$\frac{\partial c}{\partial t} = \underline{\nabla}\cdot\left(\tilde{D}\underline{\nabla}c\right) \tag{8}$$

Equations (1) through (8) are combined in order to determine the concentration of the salt, the potential in the electrolyte, and the current density. The values of material parameters used are provided in Table 1. The electrolyte, i.e. the salt and the solvent, is assumed to have the same conductance in the cathode, and in the separator, so that their differing porous nature is not taken into consideration at this point. Thus, Eqs. (1)–(8) apply seamlessly to both Regions II and III.

The solution of Eq. (1)–(8) for Regions II and III requires initial and boundary conditions. At the outset, the salt concentration and electrolyte potential are taken to be uniform at open circuit conditions, and the current density is zero.

Boundary conditions: At the boundary b of Regions I and II, i.e. between the lithium anode and the separator, the Butler–Volmer equation governs the flux of lithium ions, $J_{+,b}$, into the electrolyte, and thus the component of $F\underline{N}_+$ in the outward normal direction on the surface of the anode is equal to $J_{+,b}$, given by

$$J_{+,b} = i_{0,b}\left\{\exp\left(\frac{\alpha_{A,b}\eta_b F}{RT}\right) - \exp\left(\frac{\alpha_{C,b}\eta_b F}{RT}\right)\right\} \tag{9}$$

where the overpotential between Regions I and II at boundary b is

$$\eta_b = \Phi_{I,b} - \Phi_{II,b} - U_{Li} \tag{10}$$

The parameter $i_{0,b}$ is the exchange current density for the anode surface, and U_{Li} is the open circuit potential (OCP) of the anode. Note that $J_{+,b}$ is defined as a current density. As the anode is lithium metal and is used as the datum, or ground electrode, its OCP is zero. For this interface we take the exchange current density $i_{0,b}$ to be constant, although generally it is a function of the lithium concentration in the electrode and the adjacent electrolyte [33]. In a metallic anode, the lithium concentration is essentially invariant, and in the adjacent electrolyte remains nearly constant. Hence taking $i_{0,b}$ as a constant value for the anode is a reasonable approximation. $\alpha_{A,b}$ and $\alpha_{C,b}$ are defined as apparent transfer coefficients, kinetic parameters that govern the influence of the applied potential on reactions [26]. For this work we assume them to be equal with value 0.5.

The Butler–Volmer equation also governs the reaction occurring at boundary f, namely the insertion and extraction of lithium ions into and out of storage particles. The Li^+ ion flux into the electrolyte relative to the electrode surface overpotential is given by

$$J_{+,f} = i_{0,f}\left\{\exp\left(\frac{\alpha_{A,f}\eta_f F}{RT}\right) - \exp\left(-\frac{\alpha_{C,f}\eta_f F}{RT}\right)\right\} \tag{11}$$

$$\eta_f = \Phi_{IV,f} - \Phi_{III,f} - U_{\text{Storage Material}} \tag{12}$$

It follows that the component of $F\underline{N}_+$ in the outward normal direction from the storage particles is equal to $J_{+,f}$. The exchange current density, $i_{0,f}$, in this case depends on lithium concentration in the following way

$$i_{0,f} = Fk_R\left(c_{IV,\max} - c_{IV,f}\right)^{\alpha_{A,f}}\left(c_{IV,f}\right)^{\alpha_{C,f}} \tag{13}$$

where k_R is a constant and $c_{IV,\max}$ is a saturation value for the lithium concentration in the storage particle. Thus the flux of lithium is dependent on its concentration at the particle surface, and saturation and depletion act as limiting factors to further intercalation or de-intercalation, respectively. As a consequence, the lithium concentration in the particle is naturally deterred from violating limiting values, and thus from

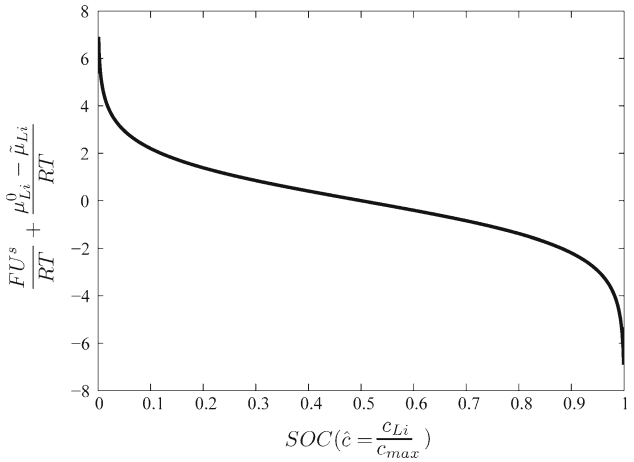

Fig. 2 A plot of the ideal OCP used for the material of the cathode storage particles

entering the range of concentrations where phase changes can occur. Note that if the particle surface is completely depleted of lithium, and insertion is taking place, entropy differences between the particle and the electrolyte are sufficiently large to overcome the sluggish aspect introduced to kinetics by the exchange current density dependence on the lithium concentration in the particle. A similar effect occurs upon extraction of lithium from a saturated particle surface.

In this work, we do not use the OCP of any particular storage material. Instead the ideal OCP as developed previously is used [24]. This OCP, U^s, is related to the ideal chemical potential, μ_{Li}, of lithium in a storage particle via the following two equations.

$$\mu_{Li} = \mu^0_{Li} + RT \ln \frac{c_{IV,f}}{c_{IV,\max} - c_{IV,f}} - \Omega_{Li}\sigma_h$$
$$0 \le c_{IV} \le c_{IV,\max} \tag{14}$$
$$FU^s(t) = \tilde{\mu}_{Li} - \mu_{Li}(r_0, t) \tag{15}$$

where μ^0_{Li} is a reference chemical potential, $c_{IV,f}$ is the concentration of lithium at the particle surface, $c_{\max}$ is the maximum permitted concentration, Ω_{Li} is the partial molar volume of lithium in the storage particle, σ_h is the hydrostatic stress at the particle surface and $\tilde{\mu}_{Li}$ is the chemical potential of lithium in a metallic electrode at ground potential. In Fig. 2 we illustrate the OCP as derived from Eq. (15), subject to Eq. (14), as a function of the state of charge (SOC) for a particle having a uniform lithium concentration, and therefore zero stress. The average value of $c_{IV}/c_{IV,\max}$ in the cathode storage particle will be termed the SOC. Strictly speaking, this terminology should be applied only to the anode, as it is filled with lithium during battery charging and depleted during discharge. Nevertheless, we will adopt this terminology for individual storage particles indiscriminately, using the term SOC as defined above for any storage particle. We take the OCP defined in Eq. (15) and illustrated in Fig. 2 as that for the cathode storage particles. As such, it is free of complicating phenomena such as phase changes, and therefore is a suitable starting point for this study.

As noted above, Li^+ ions are permitted to freely pass through interface c between the cathode and the separator. However, the surface of the current collector at d is impermeable to Li^+ions so that the flux there is zero, and as a consequence, the component of $\underline{N}_+$ normal to the current collector in the y direction is zero. Periodic boundary conditions are imposed on ion transport connecting boundaries 2–6 and 3–7. As a consequence, there is no Li^+ flux through all these boundary segments, and the component of $\underline{N}_+$ in the x direction is thus zero. In addition, parameters including potential and Li^+ concentration are required to have common values at equivalent points on boundaries 2 and 6 and 3 and 7.

The negative counterions within the electrolyte are kept entirely within Regions II and III. Therefore, interfaces b, d and f and boundaries 2, 3, 6 and 7 are all impermeable to them. Therefore, the component of $\underline{N}_-$ normal to each of these boundaries and interfaces is zero.

2.1.2 Electron transport

The current collector, shown as Region V in Fig. 1, is the location where, during discharge, electrons flow into the cathode from the external lead. The current density in this region is governed by Ohm's law

$$\underline{i}_V = -\kappa_V \underline{\nabla} \Phi_V \tag{16}$$

where $\underline{i}_V$ is the current density, κ_V is the conductance of the current collector and $-\underline{\nabla}\Phi_V$ is its electric field. We attribute a net conductance, κ_{III}, to our composite model of Region III in the cathode, representing the effective property of the percolating pathway of carbon that conveys electrons from the current collector to the storage particles. Thus, Ohm's law for electrons in the cathode is

$$\underline{i}_{III} = -\kappa_{III} \underline{\nabla} \Phi_{III} \tag{17}$$

Ohm's law for electrons in the anode (Region I), composed of lithium metal, is

$$\underline{i}_I = -\kappa_I \underline{\nabla} \Phi_I \tag{18}$$

The separator, Region II, is a non-conductor of electrons, and so its electron conductance is zero. As always, charge conservation requires the divergence of the current density throughout electron conducting regions, namely Regions I, II and III, to be zero.

Boundary conditions: Since the battery is an electrical circuit, the currents normal to boundaries a and e have the same value, designated i_{app}, taken to be positive when the battery is being charged; i.e. the current is in the positive y direction in Fig. 1 when i_{app} is positive. Lithium metal serves

as the datum electrode for the battery and therefore boundary a is set to ground, i.e. zero potential. Interfaces b and c are impermeable to electrons, so the electron current in the positive y direction is zero. However, conditions on interface b are complicated by the presence of a redox reaction there, as addressed below. Interface d is such that the electron current normal to it is continuous. Periodic conditions on boundaries 1, 3, 4, 5, 7 and 8 require the electron flux through them to be zero, so that the component of the electron current normal to all of these boundaries in the x direction is zero. These boundary conditions also impose equivalence between the potential for electrons on the paired boundaries 1 and 5, 3 and 7 and 4 and 8.

Due to the redox reactions at interfaces b and f, these surfaces act as sources or sinks for electrons, with conditions determined by the Butler–Volmer formulae in Eqs. (9) and (11) for interfaces b and f, respectively. As a consequence, the electron current orthogonal to interface b in the direction of the outward normal to the anode is given by $J_{+,b}$. Similarly, the electron current orthogonal to interface f in the direction of the outward normal to the storage particle is equal to $-J_{+,f}$. The surface potential of storage particles at interface f is required to be equal to the electric potential determined at that location from the electron flow computations in Region III.

2.1.3 Lithium diffusion and stress in storage particles

The flow of lithium ions in storage particles is governed by a coupled diffusion-stress model [23]. We provide a summary of the equations below but a more detailed description can be found in [24,25].

Our model for the chemical potential of lithium intercalated in storage particles, already referred to in Eq. (14), is

$$\mu_{Li} = \mu_{Li}^0 + RT \ln \frac{c_{Li}}{c_{\max} - c_{Li}} - \Omega_{Li}\sigma_h \qquad 0 \le c_{Li} \le c_{\max} \tag{19}$$

We do not explicitly identify Region IV as the subject domain, as it is the only component of the battery where solid-state diffusion occurs. The lithium flux, J_{Li}, in the storage particles is determined by [23]

$$\underline{J}_{-Li} = -\frac{c_{Li} D_0}{RT}\left(-\frac{c_{Li}}{c_{\max}}\right)(\underline{\nabla}\mu_{Li} + S_{Li}\underline{\nabla}T) \tag{20}$$

where D_0 is the diffusion coefficient of lithium in the particle, and S_{Li} is the partial molar entropy of lithium, i.e. the negative of the coefficient of T in Eq. (19). When combined with Eq. (19), this leads to

$$\underline{J}_{Li} = -D_0\left\{\underline{\nabla}c_{Li} - \left(1 - \frac{c_{Li}}{c_{\max}}\right)\frac{\Omega_{Li}c_{Li}}{RT}\underline{\nabla}\sigma_h\right\} \tag{21}$$

Conservation of mass then provides

$$\frac{\partial c_{Li}}{\partial t} = D_0\underline{\nabla}\cdot\left\{\underline{\nabla}c_{Li} - \left(1 - \frac{c_{Li}}{c_{\max}}\right)\frac{\Omega_{Li}c_{Li}}{RT}\nabla\sigma_h\right\} \tag{22}$$

given that D_0 is uniform. Swelling strains occur due to volume changes that arise during intercalation/deintercalation of lithium in the storage particle. When these strains are heterogeneous, elastic stress will also arise, so that the total strain is given by

$$\underline{\varepsilon} = \frac{1}{E}\left[(1+\nu)\,\underline{\sigma} - 3\nu\sigma_h\underline{I}\right] + \frac{\Omega_{Li}\left(c_{Li} - c_{Li}^0\right)}{3}\underline{I} \tag{23}$$

where ε is the strain tensor, E is Young's modulus, ν is Poisson's ratio, σ is the stress tensor, $\underline{I}$ is the identity tensor, and c_{Li}^0 is a datum concentration at which the swelling strain is considered to be zero. The equation for equilibrium of stress is given by

$$\underline{\nabla}\cdot\underline{\sigma} = 0 \tag{24}$$

Plain strain conditions are used for calculating the stress.

Boundary conditions: Boundary conditions for lithium flux are governed by the Butler–Volmer condition in Eq. (11). Thus, the outward flux of lithium at the surface of the particle is such that

$$\underline{n}\cdot\underline{J}_{Li} = \frac{J_{+,f}}{F} \tag{25}$$

For the equations governing stress, rigid body modes are eliminated by constraining the center of the particle to have zero displacement and rotation, and the surface of storage particles is traction free.

2.1.4 Charging cycle for the battery

In typical experimental studies, galvanostatic charging is implemented until a particular value of potential difference across the battery is reached, followed by potentiostatic charging. Galvanostatic charging involves a steady battery current, i_{app}, applied to the system, whereas potentiostatic charging involves the application of a steady potential difference across the battery. As noted earlier, the OCP and the exchange current density for cathode storage particles is dependent on the lithium concentration at the particle surface. Therefore, through correlation of the SOC and the potential difference during galvanostatic charging, one can make a good estimate of how much lithium is present at the surface of cathode storage particles. This feature can be used to decide when to switch from galvanostatic to potentiostatic charging to avoid overfilling surface regions of storage particles that can cause damage through side reactions and phase changes. To simulate this process, we choose to carry

out computations for galvanostatic charging until a specified potential difference across the battery is reached and to then invoke potentiostatic charging until a specified SOC is reached. In the case of our simulations, as with experiments, it is the battery current and the battery potential difference that are controlled, rather than the lithium flux rate and electric potential at the surface of storage particles, as is often the case in numerical simulations [7,19,31].

We use the OCP curve given by $-(RT/F)\ln[SOC/(1-SOC)]$ determined at room temperature. This curve derives from Eqs. (14) and (15) and has a similar profile as Fig. 2, but expressed in dimensions of volts. For our study, we carry out galvanostatic charging until a limiting potential of 0.22 V is reached, which correlates with a surface SOC of 0.00035. However, the concentration of lithium in the particle is non-uniform so that the average SOC tends to be much higher, at least as high as 0.01. Indeed, the surface SOC in the most severely depleted particle may lie significantly above 0.00035 at the time of transition due to polarization effects in the cell. As a result, a significant amount of lithium can remain to be extracted after the transition to potentiostatic charging. Therefore, we set 0.22 V as the limit to galvanostatic charging, and after it is reached, we reduce the current in order to maintain that potential; i.e. we switch to potentiostatic charging. Potentiostatic charging is carried out until the average SOC in the storage particles reaches 0.01.

In the following simulations we apply relatively high rates of charging to the particle. As a result of this the transition from galvanostatic to potentiostatic charging is reached quickly, leading to a sudden decrease in current as the charging process switches. As a result, even for small computational time steps, the potential overshoots the specified limit, leading to a termination of the simulation. In order to get through the transition, we introduce a smoothing function for the current. In lieu of reducing the current to zero, it is reduced over a range of 0.22 $\pm$0.002 V, which, in terms of SOC, represents an incremental charge of 10 parts per million. The smoothing function used is inbuilt in COMSOL 4.2 [34].

3 Methodology of simulations

These simulations were performed using COMSOL v4.2 [34], a commercially available finite element analysis software, which can be used to solve coupled partial differential equations (PDE) systems.

For the problems tackled in this work, the time-dependent solver is used. While different PDE's are used to solve for variables in different regions of the geometry, we will consider the PDE for the concentration within the storage particle. The concentration varies in time and space and can be represented by the following

$$d_a\frac{\partial c}{\partial t}+\nabla\cdot\Gamma=F \quad \text{on}\ \Omega \tag{26}$$

c is the concentration, Ω is the domain and d_a is the coefficient of time derivative. Γ is a vector and F is a scalar that can be functions of other dependent variables and time. The boundary conditions are a combination of flux or Neumann boundary conditions, which are represented by the variable G and the Dirichlet boundary conditions are represented by the variable R. COMSOL re-organizes the boundary conditions in the following manner

$$-n\cdot\Gamma=G+\frac{\partial R}{\partial c}\mu \quad \text{on}\ \partial\Omega \tag{27}$$

$$R=0 \,\text{on}\quad \partial\Omega \tag{28}$$

μ represents the Lagrange multipliers, n is the normal and $\partial\Omega$ is the boundary of the domain.

COMSOL converts all equations to the weak form [35]. The benefit of the weak form is that less regularity is required of the vector Γ. The solution vector is discretized using interpolation i.e. mapping out the solution to the nodes in the domain.

$$c_l=\sum_i C_i\varphi_i \tag{29}$$

C_i represents the value of c_l at each of the nodes and forms the components of the solution vector C. φ_i are the shape functions for the variable c_l. Each component φ_i is defined as being equal to the value of c_l when C_i is unity and all other C_i are zero [35].

A function v is chosen on Ω that belongs to a class of well behaved functions V. v is discretized following the Galerkin method i.e. using the same finite element shape functions as for the dependent variable [35].

$$v_l=\sum_i V_i\varphi_i \tag{30}$$

Multiplying Eq. (26) with v and integrating over the domain we get

$$\int_\Omega d_{al,k}\frac{\partial c_k}{\partial t}v_l dA+\int_\Omega \nabla\cdot\Gamma_l v_l dA=\int_\Omega F_l v_l dA \tag{31}$$

Applying Green's theorem to Eq. (31) and combining with Eq. (27) we get

$$\int_\Omega d_{al,k}\frac{\partial c_k}{\partial t}v_l dA=\int_{\partial\Omega}(\nabla v_l\cdot\Gamma_l+F_l v_l)dA + \int_\Omega v_l\left(G_l+\frac{\partial R_m}{\partial c_l}\mu_m\right)dS \tag{32}$$

The Lagrange multipliers can be eliminated by choosing test functions v_l such that

$$\frac{\partial R_m}{\partial c_l}v_l=0 \quad \text{on}\ \partial\Omega \tag{33}$$

This implies that the functions $c_l + v_l$ satisfy the linearized versions of the Dirichlet boundary conditions. Equation (32) can be discretized as

$$L(C, \dot{C}, t) - N_F(C, t)\Lambda = 0 \tag{34}$$

where

$$L = \int_{\partial\Omega} (\nabla v_l \cdot \Gamma_l + F_l v_l) dA + \int_{\Omega} v_l G_l dS - \int_{\Omega} d_{al,k} \frac{\partial c_k}{\partial t} v_l dA \tag{35}$$

$$N_F(C, t)\Lambda = \int_{\Omega} v_l \frac{\partial R_m}{\partial c_l} \mu_m dS \tag{36}$$

C is the solution vector, $\dot{C}$ is the time derivative, t is the time, N_F is the constraint force Jacobian and Λ are the Lagrange multipliers.

We make a note about the system of constraints R_m. In the above equations we have considered the Dirichlet boundary conditions given by Eq. 28. COMSOL further discretizes the Lagrange multipliers by modifying Eq. 28. These constraints are multiplied either by the Lagrange points (pointwise constraints) or by another set of test functions (weak constraints). This is akin to considering the Lagrange multipliers themselves as a field variable.

Therefore the equations of constraints modifies to

$$R_m v_m = 0 \tag{37}$$

where v_m represents the multipliers. These equations are collected into an equation of constraints, or the 'constraint residual' given by

$$M(C, t) = 0 \tag{38}$$

The components of L remain the same, the components of N_F and Λ will be modified accordingly by modifying the steps starting from Eq. 32.

The Jacobian of the constraints is defined as

$$N = -\frac{\partial M}{\partial C} \tag{39}$$

For ideal constraints

$$N = N_F \tag{40}$$

The IDA solver is used to solve this system [36,37] using a variable-order variable-step-size backward differentiation formula (BDF). For our problems the maximum order was set to 5 and the minimum to 1. The step size taken by the solver is unconstrained, other than by a limit of 0.5 s on the maximum step size. As the time-stepping schemes are implicit a nonlinear system of equations is solved at each time step with use of the non-linear solver inbuilt in COMSOL. The equations are linearized as follows,

$$D\dot{W} + KW = L - N_F\Lambda \tag{41}$$

$$NW = M \tag{42}$$

where $K = -dL/dC$ is the stiffness matrix and $D = -dL/d\dot{C}$ is the damping matrix. W is the linearization of the solution C that is being iterated over. As the solver goes through more iteration it gets closer to the solution. For a linear problem, you would have W = C. Once the convergence criteria is satisfied the next step is taken, the details of which are described below.

The nonlinear solver uses an affine invariant form of the damped Newton method [38]. The discrete form of the equations can be written as $f(C) = 0$ where $f(C)$ is the residual vector. The algorithm uses an initial guess C_0 as a linearization point and then extracts δC from $f'(C_0)\delta C = -f(C_0)$ using a linear solver. A new estimate is computed as $C_1 = C_0 + \lambda\delta C$ where $0 \leq \lambda \leq 1$ is the damping factor. The error E is assessed by solving $f'(C_0)E = -f(C_1)$. If the relative error corresponding to E is larger than the relative error in the previous iteration, the code reduces the damping factor and recomputes C_1. The algorithm repeats until the relative error reduces from that in the previous step or until the minimum damping factor is reached. After a successful step, the next Newton iteration occurs.

The convergence criterion governing the solver is given by the value of the error. The software stops the iterations when the relative tolerance exceeds the relative error, which is the weighted Euclidean norm.

$$e = \left(\frac{1}{N} \sum_{i=1}^{N} \left(\frac{|E_i|}{W_i} \right)^2 \right)^{1/2} \tag{43}$$

N is the number of degrees of freedom and $W_i = \max(|C_i|, S_i)$,where S_i is a scale factor determined by the solver. If $W_i = 1$ then e is an estimate for the absolute error. For these calculations the relative tolerance was set at 10^{-4} and the absolute tolerance was set at 10^{-5}. While relative error is a dimensionless number, the absolute error has the units of the dependent variable.

The linear system solver used is MUMPS: MUltifrontal Massively Parallel sparse direct Solver [39] which uses the multi-frontal approach [40]. MUMPS has a limited degree of multi-processor capability, with it being able to distribute tasks to other processors, provided a main host processor is identified. The 'Fully Coupled' Attribute was also used in this problem. This means that all the equations for all solution variables are collected in one single matrix equation, which is then solved using the MUMPS solver.

One of the benefits of using COMSOL was the presence of predefined sets of equations within various modules, with the algorithms within these modules optimized to handle these specific PDEs. The various modules used by us are as follows:

- The Nernst–Planck equations used to describe the equations of the electrolyte. These are inbuilt components of the Chemical Species Transport module.
- The electric currents component of the AC/DC module was used to model the electronic transport throughout the system.
- The PDE module was used to model the lithium diffusion within the storage particles.
- The solid mechanics component of the structural mechanics module was used to model the stress equations.

A mesh consisting of triangular elements was used. In the single particle case the total number of elements was 531, with 150 elements used for the storage particle and 124 elements used for the electrolyte. For the two particle case, 829 elements were used with 318 elements being used for the storage particles and 262 elements used for the electrolyte. Finally, 1147 elements were used in the three particle case with 494 and 416 elements being used for the storage particles and electrolyte respectively.

4 Non-dimensional parameters: derivation and range of values

In our previous work [24] we non-dimensionalized the diffusion-stress model for a single spherical particle to obtain material independent results over a range of values for the resulting non-dimensional groups of parameters. In the present work we use values of material properties from experiments for all components of the battery other than the storage particle. In view of this, we do not non-dimensionalize the system equations. However, we identify and use non-dimensional parameters relevant to the storage particles to guide us in the choice of specific values of material properties for the storage particle, so that we can undertake simulations for an interesting diversity of regimes of battery behavior. The non-dimensional parameters are defined as follows.

Following Zhang et al. [19] we use a non-dimensional surface current density given by

$$\hat{I} = \frac{i_+ r_0}{F D_0 c_{\max}} \tag{44}$$

where i_+ is a representative value of the current density at the surface of a typical storage particle during galvanostatic charging arising as a consequence of the configuration of the battery, and r_0 is the radius of a storage particle. Charge conservation and the fact that the battery is a current loop requires that the current flowing through the external battery connection is equal to the total current of Li^+ ions leaving cathode storage particles during charging. Therefore, to obtain i_+, we take the total current in the battery loop during galvanostatic charging, and divide that by the total surface area of cathode storage particles.

For a battery of unit thickness and width L as shown in Fig. 1 subject to a current density i_{app} during galvanostatic charging, and having m cylindrical cathode storage particles all of the same radius r_0, we obtain

$$\hat{I} = \frac{i_{app} L}{F D_0 c_{\max} 2\pi m} \tag{45}$$

We non-dimensionalize the partial molar volume as

$$\hat{\Omega} = \frac{\Omega_{Li} E}{RT} \tag{46}$$

and use the maximum swelling strain induced in the particle by lithium

$$\varepsilon_{Li}^{\max} = \Omega_{Li} c_{\max} \tag{47}$$

as a third dimensionless parameter.

Given that the concentration of lithium in storage particles influences transport behavior throughout the entire battery, it is best to keep that fixed through all the simulations and change the value of the other parameters entering the dimensionless groups. Hence the value of $c_{\max}$ is kept fixed throughout, and its value is taken as that of $LiMnO_4$ [7,19,31], i.e. $c_{\max} = 2.29 \times 10^4$ mol/m^3. The initial value of lithium concentration in cathode storage particles is chosen to be 95 % of $c_{\max}$. We then identify a range of values for the non-dimensional parameters in Eqs. (45)–(47) for which we wish to carry out computations, and, at room temperature, use those groups to determine the requisite values for the lithium partial molar volume, Young's modulus and the charging current density, i_{app}.

In the results we non-dimensionalize the stress tensor as follows.

$$\hat{\underline{\sigma}} = \frac{\underline{\sigma}}{E} \tag{48}$$

Previously, other authors have non-dimensionalized the stress tensor by dividing it by $\Omega_{Li} c_{\max} E$, since this group sets the scale for the stress components [21,34]. We prefer to normalize the stress tensor by Young's modulus alone, as we believe the resulting values are more informative, representing the scale of the elastic strains.

5 Results and discussion

5.1 Isolated particles

We consider first a single particle in the cathode, as illustrated in Fig. 3; however, we note that due to periodic boundary conditions, this configuration represents a row of particles parallel to the current collector, and therefore, depending on the distance separating particles, interactions among particles

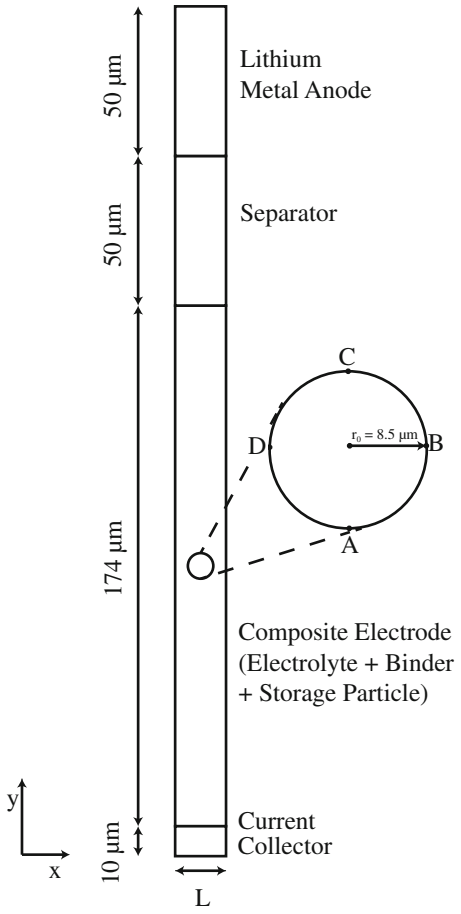

Fig. 3 A schematic of a single isolated particle in a cathode, representing a row of particles due to the use of periodic boundary conditions

may occur. We locate the row of particles half way between the current collector and the separator, as shown in Fig. 3. The width of the repeating unit of the battery, L (see Figs. 1, 3), is determined so that the smallest distance between the surfaces of particles in the same row is d_p; given a particle radius of r_0, the total width becomes

$$L = 2r_0 + d_p \tag{49}$$

The length of each segment of the battery (separator, etc.) is taken from the works of Garcia et al. [31], Doyle et al. [28] and Wang and Sastry [33]. The length of the anode and separator are 50 µm each, the length of the cathode is 174 µm and the length of the current collector is 10 µm. The particle radius is chosen to be 8.5 µm. The values of all dimensions and material properties used in the simulations are detailed in Tables 1 and 2. In view of the resulting geometry, we conclude that the cathode storage particles are spaced a large distance from the separator and the current collector, though particles in the same row can be close together. In this sense, the particles considered are isolated from other features of the battery.

For the simulations we use COMSOL v4.2 [34]. The range of values used for the non-dimensional parameters in the simulations is highlighted in Table 3. The values of the different parameters are chosen based on results from stress maps; we choose values at extremes as well as combinations of parameters that invoke different regimes of interaction between the mechanical stress and lithium concentration in storage particles; in particular, we are interested in cases where the stress gradient dominates the driving force for lithium diffusion, and, in contrast, in cases where the lithium concentration gradient dominates it.

The values of d_p are initially chosen as $2r_0$ and $r_0/2$. As mentioned in Garcia et al. [31], one of the problems of a 2-D, planar simulation is that artificial constraints are created to the motion of species in the electrolyte. Two particles that are very close to each other restrict the motion of the electrolyte (and subsequently the lithium ions) in the small gap between them. An actual, 3-D battery can have neighboring storage particles that touch each other because the species in the electrolyte can find alternative routes around the particle, reducing the severity of the consequences of particle contact. Another reason for avoiding particles that touch each other is that we do not consider the effects of contact and contact stress in this work. Therefore, we prefer to avoid situations where the swelling of particles due to lithiation is large enough to cause contact and contact stress due to constraints among the particles.

The maximum circumferential stress experienced at the surface of the cathode storage particles when they are arranged in a single row far from the current collector and the separator is shown in Fig. 4 for the different particle spacings and values of material and performance parameters. The maximum stress experienced in the particles is in the z or through thickness direction, i.e. parallel to the axis of the cylinder. We judge that the more relevant results are the circumferential stresses, as these components are analogous to those obtained for spherical particles [24]. The second principal stress is an accurate measure of the circumferential stress at the surface and this is the stress that is plotted in the following figures.

We identify the stress at Point B as shown in Fig. 3, located at a location that should show the maximum effects of particle interaction. The influence of parameters $\hat{I}$, $\hat{\Omega}$ and $\varepsilon_{Li}^{\max}$ in regard to behavior in a single particle subject to spherically symmetric lithium flux has been described in detail in [24], so we restrict ourselves to the salient results here. Figure 4a shows those for a high value of the non-dimensional current, $\hat{I} = 15$, while Fig. 4b is for a lower value, $\hat{I} = 1$. A higher charge rate leads to a higher value of stress. This is because a high rate of extraction leads to the development of a large lithium concentration gradient within the particle. A large gradient in the concentration of lithium, leading to large gradients of lithiation strain, requires a large elastic

Table 2 Value of material parameters [7,19,28,31,33]

Symbol	Parameter	Value
r_0	Particle radius	8.5 μm
D_0	Diffusion coefficient of storage particle	7.08×10^{-15} m^2/s
$c_{\max}$	Maximum concentration of lithium in the storage particle	2.29×10^4 mol/m^3
κ_{IV}	Electrical conductivity of storage particles	3.8 S/m
ρ_{part}	Density of storage particles	4140 kg/m^3
k_R	Reactivity coefficient at particle/electrolyte interface	1.9×10^{-9} m/s
$\alpha_{A,i}$	Anodic empirical constant	0.5
$\alpha_{C,i}$	Cathodic empirical constant	0.5
κ_{III}	Electrical conductivity of binder mixture	2.53 S/m
κ	Ionic conductivity of electrolyte/solvent mixture	0.108 S/m
c_{ini}	Initial value of electrolyte concentration	2000 mol/m^3
t_+^0	Transference number	0.463
D	Diffusivity of lithium in the electrolyte	7.5×10^{-11} m^2/s
κ_{II}	Electrical conductivity of lithium anode	1.08×10^7 S/m
$i_{0,b}$	Exchange current density at electrolyte anode interface	8.5×10^3 A/m^2
κ_{IV}	Electrical conductivity of nickel metal foil	1.25×10^7 S/m

Table 3 Values of the parameters used

Parameter	Values
d_p	$r_0/2$
$\hat{\Omega}$	1500, 150, 15
$\varepsilon_{Li}^{\max}$	1.0, 0.1, 0.01
$\hat{I}$	1.0, 15.0

strain in compensation and thus produces a large maximum stress [7,19]. The monotonically increasing dependence of the maximum stress on the maximum lithiation strain, $\varepsilon_{Li}^{\max}$, arises because this parameter controls all strain magnitudes, including elastic ones, in the extraction or insertion process.

The dependence of the results for stress on $\hat{\Omega}$ is complex, due to the coupling of the effects of stress and lithium concentration. The stress gradient that builds up in the storage particle will always aid the process that is being undertaken; i.e. during extraction the hydrostatic stress at the particle surface is positive, whereas at its center the hydrostatic stress is negative, thereby hastening the lithium flux. We note that the parameter $\hat{\Omega}$ controls the degree of influence that the stress gradient has on lithium flux [24]. When $\hat{\Omega} = 0$, the stress gradient has no effect on the lithium flux, whereas the stress gradient has a strong influence on lithium diffusion when $\hat{\Omega}$ has a high value. In the latter situation, when $\hat{\Omega}$ is very high, stress gradient driven diffusion can be so rapid that it counters any tendency for stress gradients to build up. Since stress gradients arise as a consequence of lithium concentration gradients, the effect of a very high value of $\hat{\Omega}$ is to limit the extent to which lithium concentration gradients can arise. However, an aspect of Eq. (21) is that the influence of the stress gradient on the lithium flux is strongest when the lithium concentration is equal to $c_{\max}/2$ and falls off for higher and lower values of c_{Li}. This combination of feature causes the history of the stress, as shown in Fig. 4, to exhibit two maxima for high values of $\hat{\Omega}$, one near the beginning of extraction and one later on when the particle approaches the stage of being fully depleted.

Simulations carried out with $d_p = 2r_0$ and $d_p = r_0/4$ did not yield any changes in the results compared to those in Fig. 4. It is clear from these and other simulations that the distance between particles has negligible effect on the stress history in the range considered.

5.2 Closely packed particles

We now consider multiple rows of particles within the cathode. During charging, the flux of lithium in the cathode is from the storage particles to the separator. As a consequence, the electric potential in the electrolyte is lower at the storage particles and higher near the separator, while electron transport from the storage particles to the current collector requires the electric potential in the storage particles to be lower in the row nearest the separator and higher in the row of particles nearest the current collector. The outcome of this situation is that lithium is extracted fastest from the row of particles nearest the separator and more slowly from the particles nearest the current collector. As a consequence, the

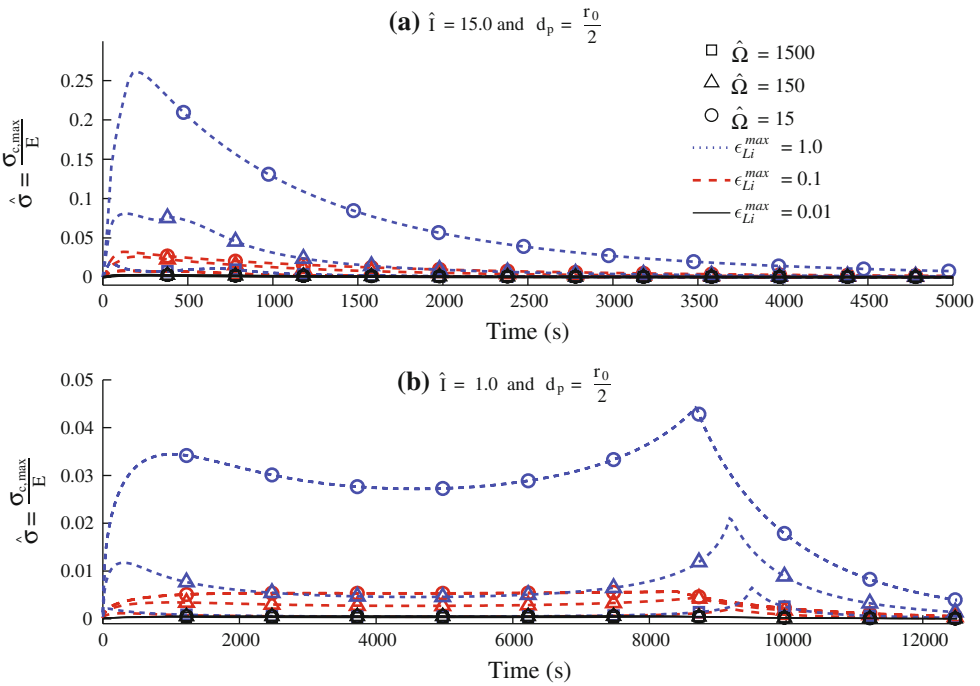

Fig. 4 History of the maximum circumferential stress in a particle in a single particle row in a cathode during charging. The stress history is shown at point B (see Fig. 3), given different charging rates and particle spacing, d_p. **a** $\hat{I} = 15$, $d_p = r_0/2$ and **b** $\hat{I} = 1$, $d_p = r_0/2$

stress in the particles nearest the separator is higher than that in the particles nearest the current collector, as has been observed by [30,31]. To examine this effect in greater detail we modify the morphology of the electrode by reducing the spacing between particles as well as the size of the electrode, without reducing the diameter of the particles. In that sense, we describe the resulting configurations as closely packed, though technically this is a misnomer as the particles are not in contact with each other.

One, two and three rows of particles, as shown in Fig. 5, are considered in this case. Note that this figure is not drawn to scale. In each case, the storage particle is located in a unit cell consisting of the particle in a square area of electrolyte, with the closest distance between the particles chosen as $d_p = r_0/4$. Therefore, the smallest distance from the particle surface to the edge of the unit cell is $r_0/8$. In Fig. 5, we have marked the particles with numbers, and various points in the particles with upper case Latin letters so that we may refer to them below.

In Fig. 6 the histories of stress and lithium concentration for a single row of particles are plotted. The time at which the transition from galvanostatic to potentiostatic charging occurs is marked as a vertical dashed line in each plot. We consider values for stress and lithium concentration at three points on the particle, (A, B and C), for various values of $\hat{\Omega}$. The maximum lithiation strain is chosen as $\varepsilon_{Li}^{\max} = 1.0$, and the non-dimensional current is $\hat{I} = 15.0$. As before, an increase in the value of $\hat{\Omega}$ leads to a decrease in the value of

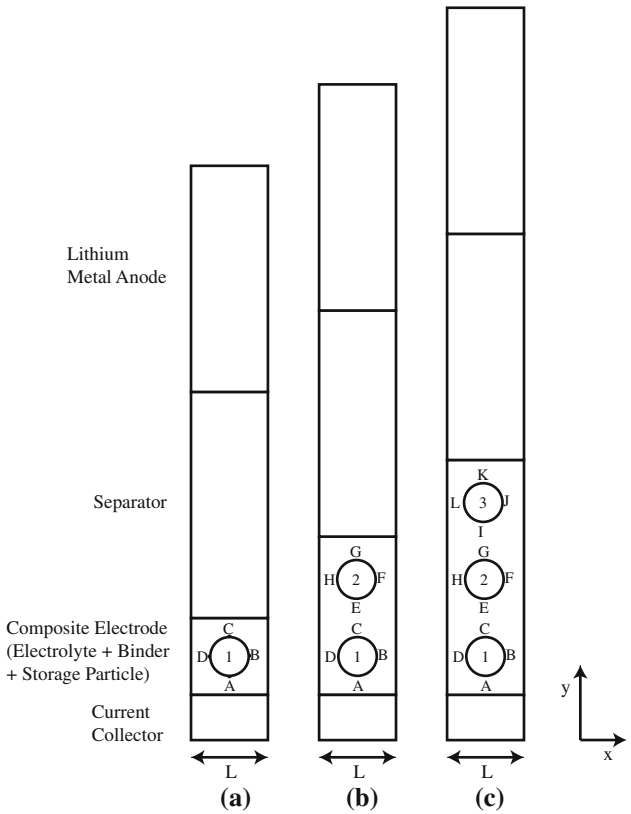

Fig. 5 A schematic of the lithium ion battery with close packed particles. Due to the periodic boundary conditions used, the configurations represent the cases of **a** one row of particles, **b** two rows, and **c** three rows

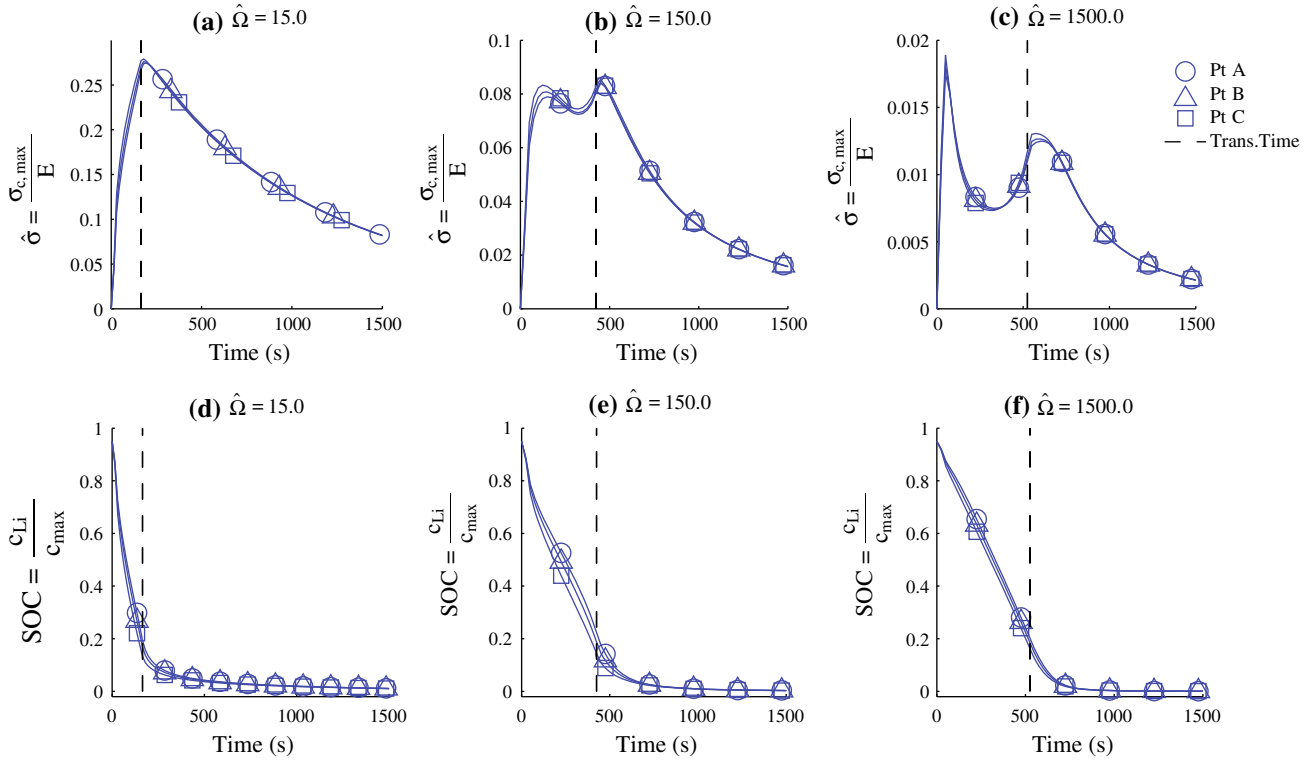

Fig. 6 The histories of maximum circumferential stress and SOC for particles in a cathode during charging for three different points on the surface of a particle in a single row in the close-packed morphology. For the positions of the three different points see Fig. 5. Parameter values are $\varepsilon_{Li}^{\max} = 1.0$, $\hat{I} = 15.0$ and $d_p = r_0/4$. Stress histories are plotted in **a**–**c** and SOC histories in **d**–**f**, such that **a** $\hat{\Omega} = 15.0$, **b** $\hat{\Omega} = 150.0$, **c** $\hat{\Omega} = 1500.0$, **d** $\hat{\Omega} = 15.0$, **e** $\hat{\Omega} = 150.0$, and **f** $\hat{\Omega} = 1500.0$

maximum stress experienced in the particle, as can be seen as we progress from Fig. 6a–c.

The variations in concentration and stress within the particle, though never great, are most pronounced for $\hat{\Omega} = 150$, as seen in Fig. 6b, e. For $\hat{\Omega} = 15$, (Fig. 6a, d) the contribution of the stress gradient to the diffusion of lithium within the particle is the least. As a result, the distribution of lithium within the storage particle is radially very non-uniform, though it is fairly uniform around the circumference, as can be seen from Fig. 6d. As a consequence of the radial non-uniformity of lithium concentration in the particle, the surface is depleted of lithium early on, and the process of charging reaches the transition between galvanostatic and potentiostatic control sooner than in the other cases. On reaching the transition point, the shift from galvanostatic charging to potentiostatic charging causes the concentration to be distributed more evenly throughout the particle, and the stress levels thereafter fall. For $\hat{\Omega} = 1500$ (Fig. 6c, f) the stress gradient contributes significantly to the diffusive flux of lithium out of the particle. As a consequence, radial gradients of lithium concentration are not able to build up, and it remains fairly uniform throughout the particle. As a result, galvanostatic extraction of lithium from the cathode storage particles can be continued longer because depletion of lithium at the particle surface is delayed. As outcomes, the transition to potentiostatic charging occurs later than in the other cases, and the stress levels are lower and fairly uniform around the particle. For $\hat{\Omega} = 150$ (Fig. 6b, e) the contribution of the stress gradient to lithium diffusion leads to a transition time between galvanostatic and potentiostatic charging that is intermediate compared to the other cases. However the influence of the stress gradient is unable to prevent the build up of large radial concentration gradients and smaller circumferential ones. We therefore see small variations of both concentration (Fig. 6e) and stress (Fig. 6b) around the particle that are more pronounced, if modest, compared to the situation observed in the other cases (Fig. 6a, c, d, f).

We now consider the system with two rows of particles, as shown in Fig. 5b. The distance between the particles is $d_p = r_0/4$ and is the same in both x and y directions. Figure 7 shows the plots of the stress and lithium concentration histories at six different points. Particle 1 (Points A, B and C) is closer to the current collector and particle 2 (Points E, F and G) is closer to the separator. The plots of the stress histories in Fig. 7a–c clearly show that particle 2 experiences steeper lithium concentration gradients and higher values of

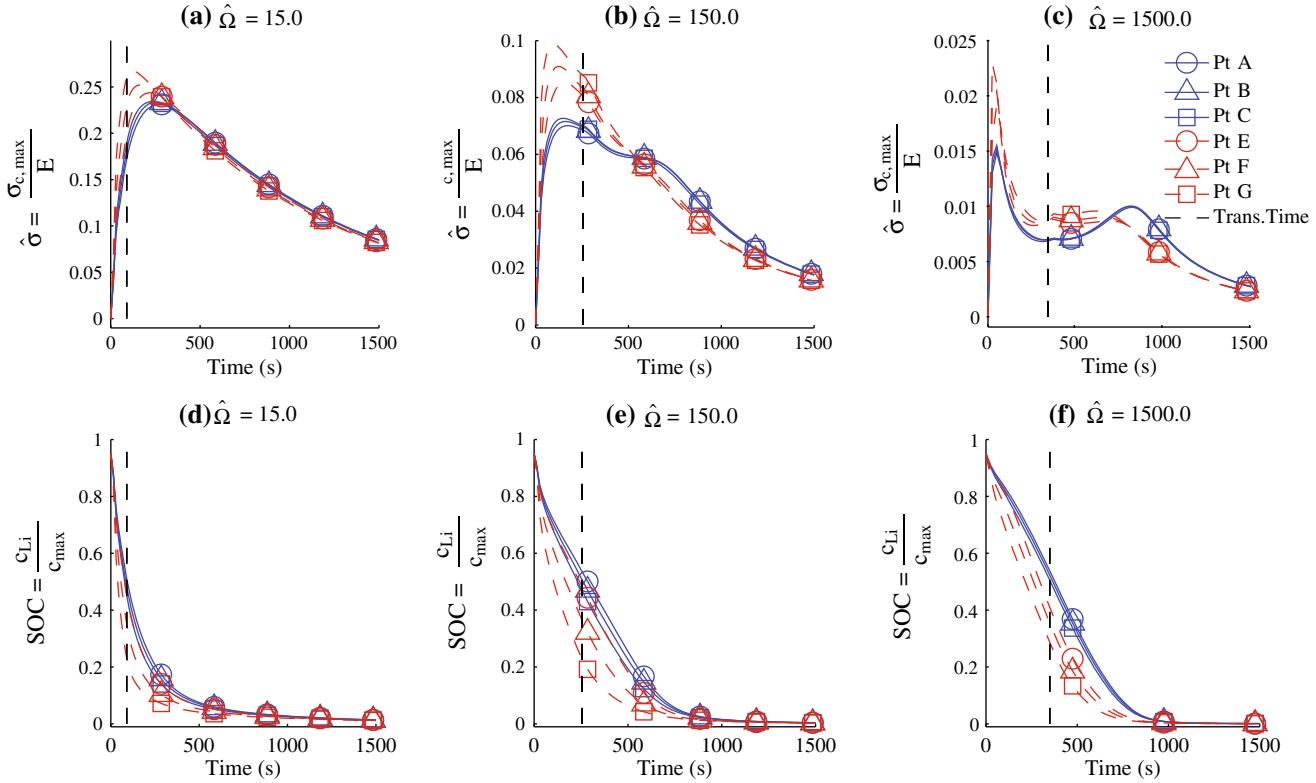

Fig. 7 The histories of maximum circumferential stress and SOC for particles in a cathode during charging for three different points on the surface of particles from each of two rows in the close-packed morphology. For the positions of the three different points on each particle see Fig. 5. Parameter values are $\varepsilon_{Li}^{max} = 1.0$, $\hat{I} = 15.0$ and $d_p = r_0/4$. Stress histories are plotted in **a**–**c** and SOC histories in **d**–**f**, such that **a** $\hat{\Omega} = 15.0$, **b** $\hat{\Omega} = 150.0$, **c** $\hat{\Omega} = 1500.0$, **d** $\hat{\Omega} = 15.0$, **e** $\hat{\Omega} = 150.0$, and **f** $\hat{\Omega} = 1500.0$

stress than particle 1. The maximum stress for $\hat{\Omega} = 15$ is similar to that for the case where there is a single row of particles (Fig. 6a). However, for $\hat{\Omega} = 150$ and 1500, the value of maximum stress increases compared to that for a single row of particles. For all three values of $\hat{\Omega}$, the level of stress experienced by particle 1 (i.e. in the row further from the separator) is lower than that for the case of a single row of particles. This fact, coupled with the observation that the lithium concentration for points on particle 2 are lower than that for particle 1, indicates that particle 2 (nearer the separator) experiences a higher extraction rate than particle 1. The cause for this is the feature that the limited ionic conductivity in the electrolyte causes a difference in the overpotential at the surfaces of the two rows of particles. Consequently, the extraction rates for the two rows are different, with the row nearest the separator being depleted of lithium faster. Within the particles in the system having two rows, the stress averages to approximately the same value as the stress in the system having a single row, but the distribution of stress levels around the particle at the different surface points is wider. We note that in the system having two rows of particles, the fluctuation of the maximum stress in time is smoother than that occurring when there is one row of particles.

In Fig. 8 the stress and lithium concentration histories for a system with three rows of particles are plotted for $\hat{I} = 15.0$ and $\varepsilon_{Li}^{max} = 1.0$. The results are similar to those of the system with two rows of particles, with points I, J and K on particle 3, which is closest to the separator, experiencing maximum stress in the system. The stress histories of points on particles 1 (A, B and C) and 2 (E, F and G) are similar to each other and have significantly lower maximal values than particle 3. For $\hat{\Omega} = 1500$ the maximum value of stress of particle 1 (furthest away from the separator) is around 55 % lower than the maximum stress in particle 3 (closest to the separator). The particle closest to the separator, i.e. particle 3, seems to act somewhat like a filter for the system. Due to the higher extraction rates at the surface of this particle, the extraction rates, and therefore the stress, at the surface of the particles further from the separator are lower. Inspection of the results for stress in the case of one, two and three rows of particles reveals a pattern. As each extra row is added, the maximal stress in the particle row nearest the separator goes up and the stress in the remaining rows goes down.

This pattern is apparent in the lithium extraction rate as well, and, of course, leads to the outcome in terms of stress just described. That is, as each row of particles is added, the

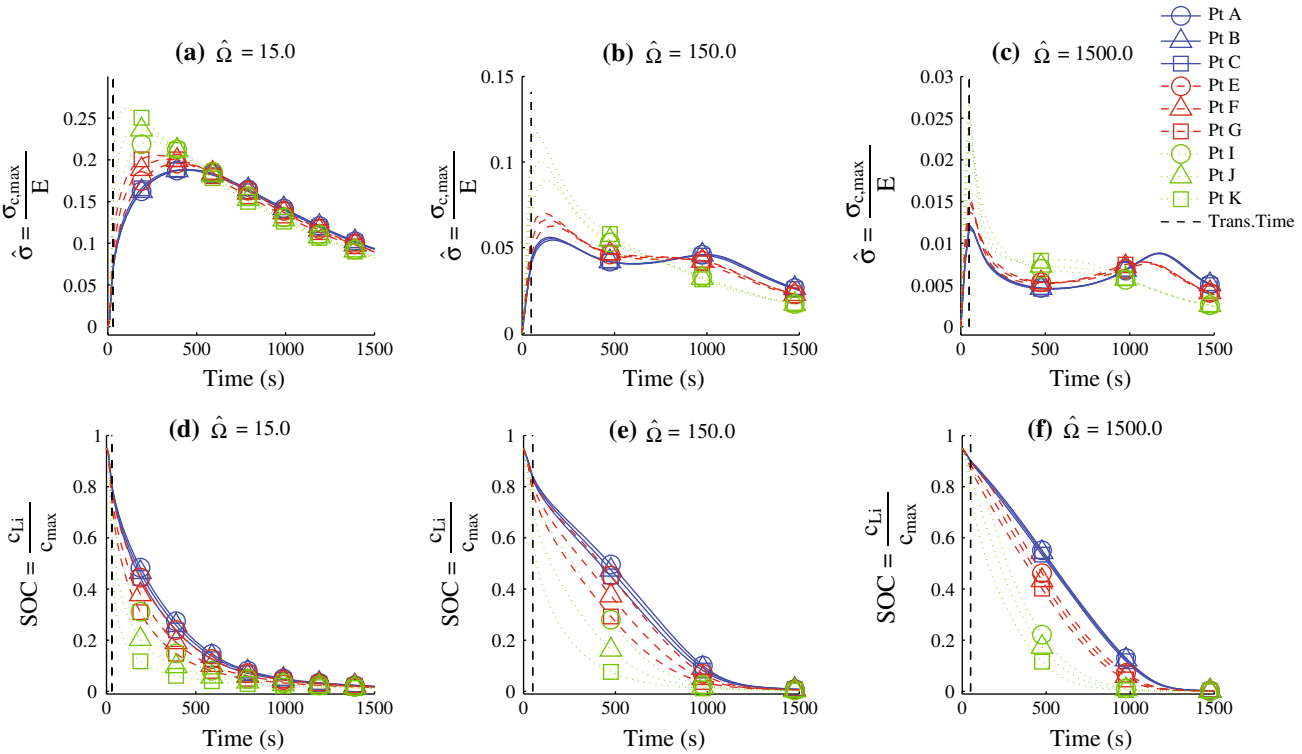

Fig. 8 The histories of maximum circumferential stress and SOC for particles in a cathode during charging for three different points on the surface of particles from each of three rows in the close-packed morphology. For the positions of the three different points on each particle see Fig. 5. Parameter values are $\varepsilon_{Li}^{max} = 1.0$, $\hat{I} = 15.0$ and $d_p = r_0/4$. Stress histories are plotted in **a**–**c** and SOC histories in **d**–**f**, such that **a** $\hat{\Omega} = 15.0$, **b** $\hat{\Omega} = 150.0$, **c** $\hat{\Omega} = 1500.0$, **d** $\hat{\Omega} = 15.0$, **e** $\hat{\Omega} = 150.0$, and **f** $\hat{\Omega} = 1500.0$

lithium extraction rate in the row nearest the separator goes up and that in the remaining rows goes down. As a result of this imbalance, the lithium concentration at the surface of particles in the row nearest the separator reaches the limiting value for galvanostatic charging more quickly, triggering a faster change to potentiostatic charging for the whole battery. Thus when the number of rows of particles is increased, the time elapsed until the transition from galvanostatic to potentiostatic charging is reduced, in many cases causing most of the lithium extraction for the entire cathode to occur under potentiostatic charging.

In Fig. 9 we show color contour plots of SOC in (a) and (c) and circumferential stress in (b) and (d) for a system with three rows of particles with $\hat{\Omega} = 150$, $\hat{I} = 15.0$ and $\varepsilon_{Li}^{max} = 1.0$. Figure 9a, b is plotted at t = 75 s which is the time for the transition from galvanostatic charging to potentiostatic charging, as well as the point of maximum stress in particle 3 i.e. the particle closest to the separator. Figure 9c, d is plotted at t = 1000 s, which has no special significance other than to show the effects of long term potentiostatic charging. Figure 9a indicates the significant variation in the concentration within the different particles, with most of the extraction being associated with particle 3. Particle 1, furthest away from the separator, has not experienced rapid extraction, with its center still at a lithium concentration close to its initial value. Figure 9b, the contour plot of the second principal stress at this time, highlights the effect of these concentration differences, with larger tensile stresses developing at the surface of particle 3 in comparison to particle 1. Figure 9c, d, in contrast, shows smaller fluctuations of concentration within the particle as well as lower values of stress. After undergoing potentiostatic charging for some time, the particle has begun to experience an evening out of its lithium concentration, which leads to a reduction in the stress within it.

We note that the SOC at the particle surface at t = 1000 s is significantly higher than the value that we set as the limiting value of the SOC, and that supposedly caused the transition from galvanostatic to potentiostatic charging. Indeed, at t = 75 s, when the transition took place, the surface SOC in the most severely depleted particle is around 0.5, as can be seen in Fig. 9a. As mentioned earlier, practically, it is the voltage and current at the current collector that can be controlled, not those at the particle surface, and thus the potential difference across the entire cell is used to make the decision to transition from galvanostatic to potentiostatic charging. Due to losses in the cell (both polarization losses at the interfaces subject to Butler–Volmer kinetics, and ohmic losses in the

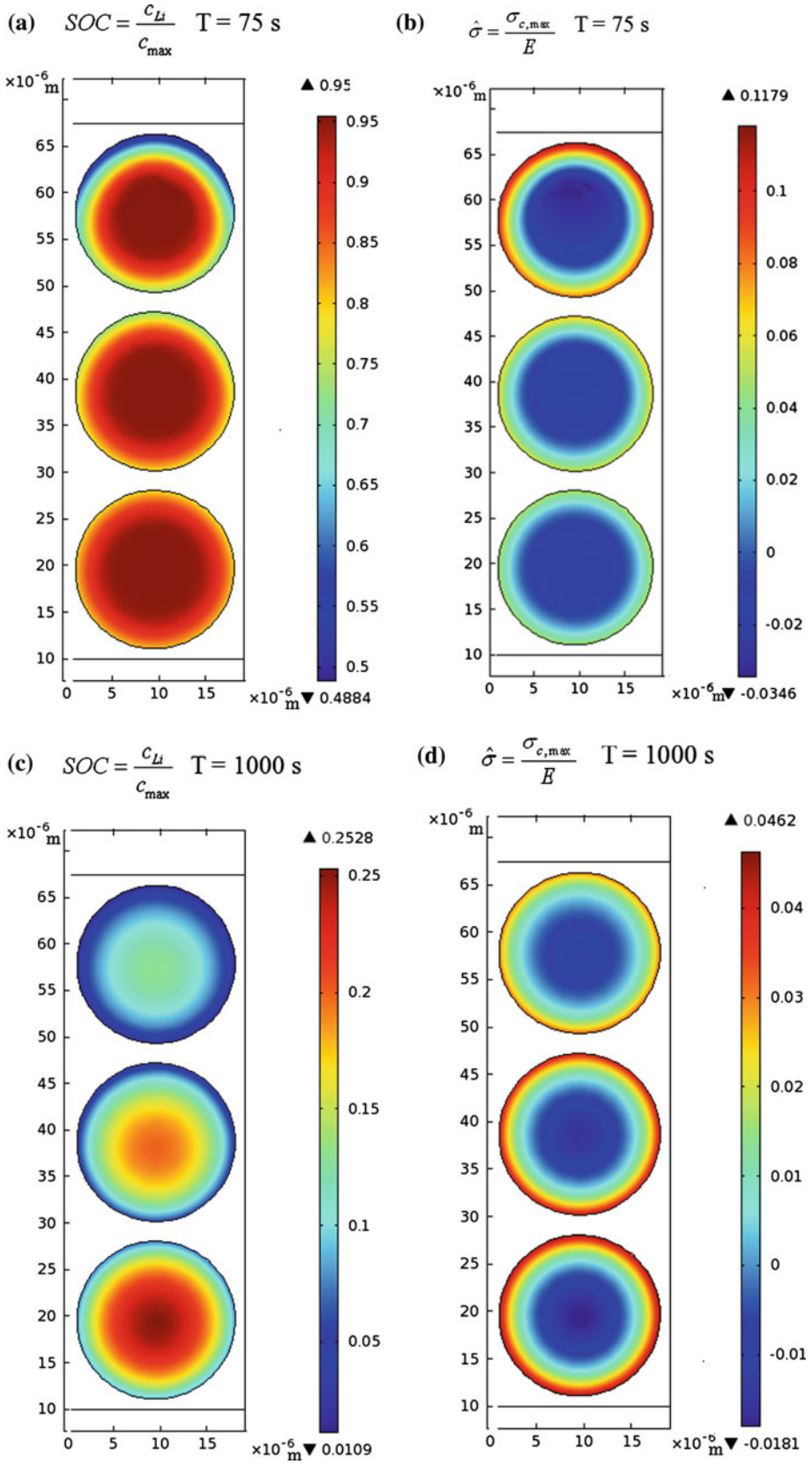

Fig. 9 Color contour plots of the maximum circumferential stress and SOC in storage particles at two different times during charging in a cathode having three rows of particle. Simulations are carried out using the following parameter values: $\hat{\Omega} = 150$, $\hat{I} = 15.0$ and $\varepsilon_{Li}^{max} = 1.0$. **a** Color contour plot of SOC at t = 75 s after the beginning of charging when the stress is maximal and the transition from galvanostatic to potentiostatic charging occurs. **b** Color contour plot of circumferential stress at t = 75 s after the beginning of charging when the stress is maximal and the transition from galvanostatic to potentiostatic charging occurs. **c** Color contour plot of SOC at t = 1000 s after the beginning of charging. **d** Color contour plot of circumferential stress at t = 1000 s after the beginning of charging

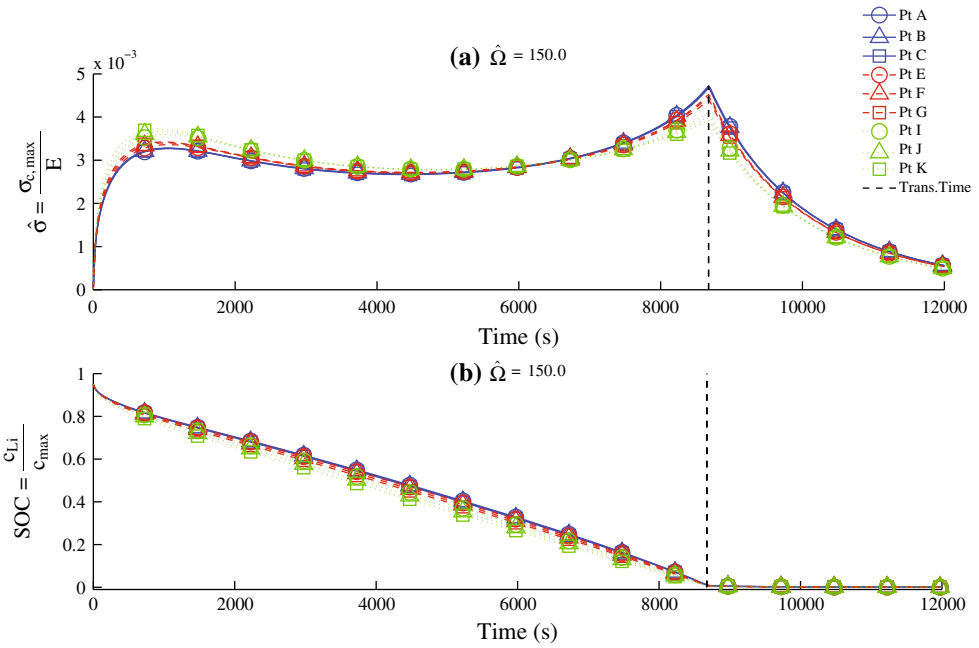

Fig. 10 The histories of maximum circumferential stress and SOC for particles in a cathode during charging for three different points on the surface of particles from each of three rows in the close-packed morphology. For the positions of the three different points on each particle see Fig. 5. Parameter values are chosen to represent lithium manganate and are $\hat{\Omega} = 150.0$, $\varepsilon_{Li}^{\max} = 0.1$, and $\hat{I} = 1.0$ with particle spacing given by $d_p = r_0/4$. Stress history is plotted in **a** and SOC history in **b**

electrolyte and electronic circuitry), the value of the voltage difference across the entire battery never matches the that of the potential at the surface of cathode particles. Hence the SOC at a cathode particle surface can remain significantly higher than the limiting value at which the charging transition is supposed to occur. The result is apparent in Fig. 9a at t = 75 s when the transition occurs in the system with three rows of particles, and where the lowest surface SOC, in the particle nearest the separator, is 0.4884, well above 0.00035. However, once the transition is enforced, potentiostatic charging is continued and we do not return to galvanostatic charging, even though the surface SOC in particles is well above the value of 0.00035 at which the transition is supposed to take place. At t = 1000 s (Fig. 9d), long after the transition from galvanostatic to potentiostatic charging, the lithium concentration at the surface of the three particles is almost identical, and is now down to approximately 0.01, much closer to the transition threshold of 0.00035.

We note that the cathode consisting of three rows of particles begins to approach the dimensions and configuration of a very thin battery electrode. In view of this, we consider a case having three rows of particles with parameters consistent with an actual storage particle material. For lithium manganate, $\hat{\Omega} = 141$ and $\varepsilon_{Li}^{\max} = 0.08$ [24]. Thus, we simulate a case having $\hat{\Omega} = 150$ and $\varepsilon_{Li}^{\max} = 0.1$ at a modest extraction rate of $\hat{I} = 1.0$. This rate corresponds to a C-Rate 0.35C assuming galvanostatic charging throughout, and to around 0.28C if we consider potentiostatic charging as well. This rate is fairly low and is representative of a low power battery, whereas a C-Rate of 1 (i.e. complete charging of the battery in an hour) is considered to be a desirable, though unambitious objective. Results are shown in Fig. 10. In Fig. 10a we see that the stresses are lower than in the previous cases due to the combined effect of a reduced $\varepsilon_{Li}^{\max}$ and a lowered $\hat{I}$. The double peaked structure in the stress history reappears, indicating a significant contribution of the stress gradient to the lithium flux. Stress differences among the particle rows are present, but are not very large. The SOC of the particles in different rows are almost the same, as can be seen in Fig. 10b. The stress remains fairly steady throughout lithium extraction until the transition from galvanostatic to potentiostatic charging is reached, and then falls gradually, as expected. Around 90 % of the lithium has been extracted when the transition is reached, i.e. almost all of it is withdrawn under galvanostatic charging.

When we add rows of particles to the system, the increase in the thickness of the cathode creates longer diffusion paths for the species in the electrolyte. To study the effect of this change, we increase the distance between particles to $d_p = r_0/2$ in a system with three rows of particles, thereby making the cathode thicker. Figure 11a, b is plots of the stress and SOC histories for the case where $\hat{\Omega} = 1500$, $\varepsilon_{Li}^{\max} = 1.0$ and $\hat{I} = 15.0$. Comparing these to Fig. 8c, f respectively, we notice that the maximum stress experienced by points on particle 3 (I, J and K) is approximately 10 % lower than for the thinner cathode where $d_p = r_0/4$. In the other two

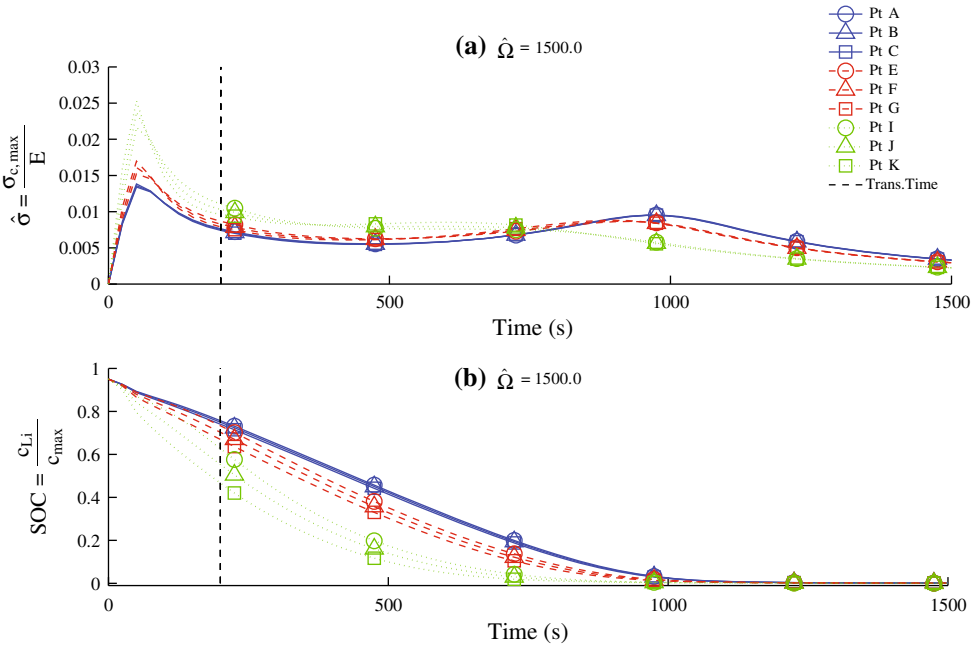

Fig. 11 The histories of maximum circumferential stress and SOC for particles in a cathode during charging for three different points on the surface of particles from each of three rows in the close-packed morphology. For the positions of the three different points on each particle see Fig. 5. Parameter values are $\hat{\Omega} = 1500.0$, $\varepsilon_{Li}^{max} = 1.0$, and $\hat{I} = 15.0$ with particle spacing given by $d_p = r_0/2$, so that the cathode is relatively thick. Stress history is plotted in **a** and SOC history in **b**

particle rows further away from the separator, i.e. particles 1 and 2, the maximal stress in the thicker cathode increases by 15 and 6 % respectively compared to the equivalent value in the thinner cathode. The time at which the transition from galvanostatic to potentiostatic charging occurs shifts from 50 s after charging begins in the thinner cathode to 200 s in the thicker one. The lithium concentrations are mostly similar, other than modest differences within with particle 3, indicating a more even distribution. It is likely that the larger particle spacing in the thicker cathode causes the distribution of the various species in the electrolyte to be more uniform, leading to smaller differences in overpotential at the surfaces of the various particles. It is important to note that in a 2-D simulation these effects are likely to be magnified, as flow-path constrictions in a 2-D system might be enough to restrict transport significantly, but in a 3-D arrangement of equiaxed particles, alternative routes would be available [31]. Hence it is possible that the differences among particles that we observe in stress in the three row system analyzed in a planar 2-D configuration would be reduced in a simulation in 3-D having equiaxed particles.

6 Concluding comments

In this work we develop a model for a 2-D lithium ion battery, including the equations of transport in the electrolyte for the various electrochemical species involved. These equations are then integrated with a previously developed coupled lithium diffusion-stress model for cathode storage particles. The system of equations is then solved to predict the transport of lithium and electrons within the battery during charging. The stress generated by shrinkage of cathode storage particles during lithium extraction is shown to increase as the charging rate is increased, to increase with the magnitude of the swelling, and to decrease as the magnitude of the product of the storage material elastic modulus and its lithium partial molar volume is increased. As expected, particle arrangement with respect to the separator is critical to the stress history experienced by storage material, with the particles closest to the separator going through the most severe conditions. The number of particles through the thickness of the electrode is shown to influence the maximal stress, with a larger number of rows of particles being detrimental. Storage material properties are shown to influence the maximal stress experienced by particles. Thus, careful design of the electrode and choice of storage material can help to alleviate the maximum stresses developed within storage particles.

Acknowledgements The research in this paper is supported by a contract with the Robert Bosch Corporation and a grant from the University of California Discovery Program. We would like to thank Dr. Esther Bohn, Dr. Niko Dorsch and Dr. Thomas Eckl of Robert Bosch GmbH, Stuttgart, for their comments and guidance. We would also like to thank

COMSOL for use of its license during November and December 2010 at Robert Bosch GmbH, Stuttgart.

References

1. Huggins RA (2009) Advanced batteries: materials science aspects. Springer, New York
2. Tarascon JM, Armand M (2001) Issues and challenges facing rechargeable batteries. Nature 414:359–367
3. Vetter J, Novak P, Wagner MR, Veit C, Moeller KC, Besenhard JO, Winter M, Wohlfahrt-Mehrens M, Vogler C, Hammouche A (2005) Ageing mechanisms in lithium-ion batteries. J Power Sources 147:269–281
4. Broussely M (2002) Ageing mechanisms and calendar-life predictions. In: van Schalkwijk W, Scrosati B (eds) Advances in lithium-ion batteries. Kluwer Academic/Plenum, New York, pp 393–432
5. Bloom I, Cole BW, Sohn JJ, Jones SA, Polzin EG, Battaglia VS, Henriksen GL, Motloch CG, Richardson R, Unkelhaeuser T, Ingersoll D, Case HL (2001) An accelerated calendar and cycle life study of Li-ion cells. J Power Sources 101:238–247
6. Nazri GA, Pistoia G (eds) (2004) Lithium batteries: science and technology. Kluwer, Boston
7. Christensen J, Newman J (2006) A mathematical model of stress generation and fracture in lithium manganese oxide. J Electrochem Soc 153:A1019–A1030
8. Christensen J, Newman J (2006) Stress generation and fracture in lithium insertion materials. J Solid State Electrochem 10(5): 293–319
9. Taberna L, Mitra S, Poizot P, Simon P, Tarascon JM (2006) High rate capabilities of Fe_3O_4-based Cu nano-architectured electrodes for lithium-ion battery applications. Nature Mater 5:567–573
10. Verbrugge MW, Koch BJ (2006) Modeling lithium intercalation of single-fiber carbon microelectrodes. J Electrochem Soc 143:600–608
11. Aifantis KE, Dempsey JP (2005) Stable crack growth in nanostructured Li-batteries. J Power Sources 143:203–211
12. Zhao K, Pharr M, Vlassak JJ, Suo Z (2010) Fracture of electrodes in lithium-ion batteries caused by fast charging. J Appl Phys 108:073517-1–073517-6
13. Yang F (2010) Insertion-induced breakage materials. J Appl Phys 108:073536-1–073536-5
14. Cheng YT, Verbrugge MW (2010) Application of Hasselman's crack propagation model to insertion electrodes. Electrochem Solid State Lett 13:A128–A131
15. Woodford WH, Chiang YM, Carter WC (2010) 'Electrochemical shock' of intercalation electrodes—A fracture mechanics analysis. J Electrochem Soc 157:A1052–A1059
16. Bhandakkar TK, Gao H (2010) Cohesive modeling of crack nucleation under diffusion induced stresses in a thin strip: Implications on the critical size for flaw tolerant battery electrodes. Int J Solid Struct 47:1424–1434
17. Bhandakkar TK, Gao H (2011) Cohesive modeling of crack nucleation in a cylindrical electrode under axisymmetric diffusion induced stresses. Int J Solid Struct 48:2304–2309
18. Hu Y, Zhao X, Suo Z (2010) Averting cracks caused by insertion reaction in lithium-ion batteries. J Mater Res 25(6):1007–1010
19. Zhang X, Shyy W, Sastry AM (2007) Numerical simulation of intercalation-induced stress in Li-ion battery electrode particles. J Electrochem Soc 154:A910–A916
20. Park J, Lu W, Sastry AM (2011) Numerical simulation of stress evolution in lithium manganese dioxide particles due to coupled phase transition and intercalation. J Electrochem Soc 158: A201–A206
21. Cheng YT, Verbrugge MW (2010) Diffusion–induced stress, interfacial charge transfer, and criteria for avoiding crack initiation of electrode particles. J Electrochem Soc 157:A508–A516
22. Cheng YT, Verbrugge MW (2009) Evolution of stress within a spherical insertion electrode particle under potentiostatic and galvanostatic operation. J Power Sources 190:453–460
23. Bohn E, Eckl T, Kamlah M, McMeeking RM (2011) A model for lithium diffusion and stress generation in a storage particle of an intercalation electrode. J Electrochem Soc (in review)
24. Purkayastha R, McMeeking RM (2012) A linearized model for lithium ion batteries and maps for their performance and failure. J Appl Mech 79, 031021-1–16. doi:10.1115/1.4005962
25. Purkayastha R, McMeeking RM (2012) A parameter study of intercalation of lithium into storage particles in a lithium ion battery (in revision)
26. Thomas KE, Darling RM, Newman J (2002) Mathematical modeling of lithium batteries. In: van Schalkwijk W, Scrosati B (eds) Advances in lithium-ion batteries. Kluwer Academic/Plenum, New York pp 345–392
27. Doyle M, Fuller TF, Newman J (1993) Modeling of galvanostatic charge and discharge of the lithium/polymer/insertion cell. J Electrochem Soc 140:1526–1533
28. Doyle M, Newman J, Gozdz A, Schmutz C, Tarascon JM (1996) Comparison of modeling predictions with experimental data from plastic lithium ion cells. J Electrochem Soc 143:1890–1903
29. Renganathan S, Sikha G, Santhanagopalan S, White RE (2010) Theoretical analysis of stresses in a lithium ion cell. J Electrochem Soc 157:A155–A163
30. Christensen J (2010) Modeling diffusion induced stress in Li-ion cells with porous electrodes. J Electrochem Soc 157:A366–A380
31. Garcia RE, Chiang YM, Carter WC, Limthongkul P, Bishop CM (2005) Microstructural modeling and design of rechargeable lithium-ion batteries. J Electrochem Soc 152:A255–A263
32. Garcia RE, Chiang YM (2007) Spatially resolved modeling of microstructurally complex battery architectures. J Electrochem Soc 154:A856–A864
33. Wang CW, Sastry AM (2007) Mesoscale modeling of a li-ion polymer cell. J Electrochem Soc 154(11):A1035–A1047
34. Comsol multiphysics user's guide, Version 4.2 (2011)
35. Cook R, Malkus D, Plesha M, Witt R (2007) Concepts and applications of finite element analysis, 4th edn. Wiley, Hoboken
36. Hindmarsh AC, Brown PN, Grant KE, Lee SL, Serban R, Shumaker DE, Woodward CS (2005) SUNDIALS: suite of nonlinear and differential/algebraic equation solvers. ACM Trans Math Softw 31:363
37. Brown PN, Hindmarsh AC, Petzold LR (1994) Using Krylov methods in the solution of large-scale differential-algebraic systems. SIAM J Sci Comput 15:1467–1488
38. Deuflhard P (1974) A modified Newton method for the solution of ill-conditioned systems of nonlinear equations with application to multiple shooting. Numer Math 22:289–315
39. http://graal.ens-lyon.fr/MUMPS/. Accessed May 5 2012
40. Amestoy PR, Duff IS, L'Excellent J-Y (2000) Multifrontal parallel distributed symmetric and unsymmetric solvers. Comput Methods Appl Mech Eng 184:501–520